IL NUOVO CIMENTO Vol. 33 C, N. 1 Gennaio-Febbraio 2010
DOI 10.1393/ncc/i2010-10565-5

Colloquia: ICTT2009

High-order discrete ordinate transport in hexagonal geometry: A new capability in ERANOS

R. Le Tellier, C. Suteau, D. Fournier and J. M. Ruggieri

CEA Cadarache, DEN/DER/SPRC/LEPh - Building 230, 13108 Saint Paul-lez-Durance France

(ricevuto il 23 Ottobre 2009; approvato il 13 Gennaio 2010; pubblicato online il 2 Marzo 2010)

Summary. — This paper presents the implementation of an arbitrary order discontinuous Galerkin scheme within the framework of a discrete ordinate solver of the neutron transport equation for nuclear reactor calculations. More precisely, it deals with non-conforming spatial meshes for the 2D and 3D modeling of core geometries based on hexagonal assemblies. This work aims at improving the capabilities of the ERANOS code system dedicated to fast reactor analysis and design. Both the angular quadrature and spatial scheme peculiarities for hexagonal geometries are presented. A particular focus is set on the spatial non-conforming mesh and variable order capabilities of this scheme in anticipation to the development of spatial adaptiveness algorithms. These features are illustrated on a 3D numerical benchmark with comparison to a Monte Carlo reference and a 2D benchmark that shows the potential of this scheme for both h- and p-adaptation.

PACS 89.30.Gg – Nuclear fission power.
PACS 28.20.Gd – Neutron transport: diffusion and moderation.
PACS 28.41.Ak – Theory, design, and computerized simulation.

1. – Introduction

We present in this paper a numerical scheme for the modeling of core geometries based on hexagonal assemblies recently introduced in the ERANOS code system [1] dedicated to fast reactor analysis.

The modeling of nuclear reactors based on hexagonal assemblies have been the subject of many dedicated developments in the past as it is a geometry of interest for both fast breeder reactors and high conversion light water reactors. Unstructured mesh-based discretizations have also been used to model such geometries. Many methods are based on the diffusion or simplified spherical harmonics angular approximation of the transport equation combined with various spatial approximations. For example, in the VARIANT code [2], a component of the ERANOS code system, a nodal spatial scheme defined over the complete hexagon is used while in [3,4], Galerkin schemes based on the discretization of the hexagons in lozenges are proposed. Such methods are part of the legacy codes

which have been used for the design and safety studies of reactors in the last past decades. However, such low-order angular transport approximations have been questioned for the precise calculation of local transport effect (*e.g.*, coolant voiding in a sodium-cooled fast reactor) and higher-order transport methods may be required to meet the accuracy targets for the design of fourth-generation reactors. For fast spectra, in most cases, because of the axial heterogeneity of the core (*e.g.*, the presence of axial reflector and blanket), a 2D plane hexagonal modeling is not adequate and a 3D hexagonal-z model is required. In view of the computational burden associated to 3D transport methods, it is the discrete ordinate (S_N) transport approximation that has received the most attention for this purpose. For instance, nodal schemes, either over the complete hexagon [5] or over six equilateral triangular nodes partitioning the hexagon [6] have been developed. Unstructured meshes of triangles (2D) or tetrahedrons (3D) with either a nodal scheme [7] or a Discontinuous Galerkin (DG) scheme [8-10] have also been introduced. With the noticeable exception of [10] (but limited to 2D), these discretizations are based on a low-order scheme in each cell and only offer conforming h-refinement capabilities (*i.e.* the triangles or tetrahedrons can be split in a conforming fashion).

Our work intends to go one step forward by developing a discrete ordinate method combined with a Discontinuous Galerkin scheme over quadrangles (2D) or hexahedrons (3D) for non-conforming meshes with arbitrary and non-uniform scheme order. This paper follows the work reported in [11] which presents a first implementation of these combined methods for 2D non-conforming Cartesian meshes. It is focused on the peculiarities of this approach when treating geometries based on hexagonal assemblies and the interested reader is referred to this previous paper for a qualitative comparison of this spatial scheme with respect to the variety of other schemes which have been developed in the discrete ordinate transport framework.

The outline of this paper is as follows. Section **2** is devoted to the presentation of the discrete ordinate method applied to hexagonal configurations. In sect. **3**, the Discontinuous Galerkin scheme is briefly presented and the choice of the arbitrary order polynomial basis is discussed. In sect. **4**, some numerical results are presented along with concluding remarks in sect. **5**.

2. – The discrete ordinate method in hexagonal geometries

2˙1. *The discrete ordinate transport equation.* – In this transport approximation, any angular integral is calculated using a quadrature rule defined over the unit sphere. The points and weights of such a quadrature are denoted $\vec{\Omega}_n$ and w_n, respectively. In this way, the linear neutron transport problem is formulated as a set of coupled first-order hyperbolic linear equations. More precisely, for a given energy group and quadrature point $\vec{\Omega}_n$, the neutron flux along $\vec{\Omega}_n$, $\phi_n(\vec{r}) = \phi(\vec{r}, \vec{\Omega}_n)$, obeys, $\forall \vec{r} \in \boldsymbol{\mathcal{D}}$,

$$\vec{\Omega}_n \cdot \vec{\nabla}\phi_n(\vec{r}) + \Sigma_t(\vec{r})\phi_n(\vec{r}) = Q_n(\vec{r}), \tag{1}$$

where $\Sigma_t(\vec{r})$ is the macroscopic total cross-section and $Q_n(\vec{r}) = Q(\vec{r}, \vec{\Omega}_n)$ is the neutron source in the fixed direction, containing external and fission sources as well as those resulting from the scattering from other directions. The associated boundary conditions are, $\forall \vec{r} \in \Gamma_-$,

$$\phi_n(\vec{r}) = \phi_n^{\mathrm{BC}}(\vec{r}), \tag{2}$$

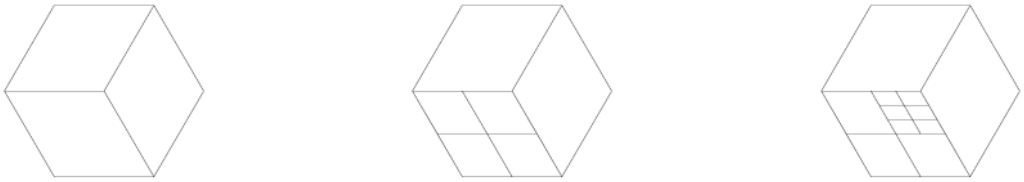

Fig. 1. – Three-lozenge–based discretization of the hexagon with local Cartesian refinements.

where the inflow boundary Γ^- of $\boldsymbol{\mathcal{D}}$ is defined by $\Gamma^- = \{\vec{r} \in \Gamma \,:\, \vec{\Omega}_n \cdot \vec{n}(\vec{r}) < 0\}$ and $\vec{n}(\vec{r})$ is the unit outward normal vector to Γ at $\vec{r} \in \Gamma$.

2˙2. *The S_N angular quadrature.* – Standard level-symmetric quadrature sets (see [12]) are defined on an octant of the unit sphere, *i.e.* for $\{\varphi \in]0, \pi/2[\} \times \{\mu \in]0, 1[\}$ where φ is the azimuthal angle and μ is the polar angle cosine. Such quadratures do not comply with the azimuthal symmetries encountered for hexagon-based geometries; consequently, artificial asymmetries in the flux are created for low-order quadrature and, more importantly, rotation boundary conditions (used for $\frac{1}{6}$, $\frac{1}{3}$ symmetries) cannot be accounted for exactly.

To overcome these two drawbacks, we have introduced a product quadrature constructed by symmetry from an azimuthal quadrature based on a N_a-point Gauss-Chebychev rule on $]0, \pi/3[$ and a polar quadrature based on a N_p-point Gauss-Legendre rule on $]0, 1[$. It is denoted HQ_{N_a,N_p} and has $12 \times N_a \times N_p$ points over the complete unit sphere. Obviously, it complies with the hexagon symmetries. Moreover, it ensures the exact integration of the real spherical harmonics orthogonality properties up to $L = \min(\frac{3}{2}(2N_a - 1), (N_p + 1))$; this result can easily be obtained following the approach presented in [13]. This property is mandatory to ensure the proper calculation of anisotropic scattering source contribution.

3. – Discontinuous Galerkin discretization

3˙1. *Spatial mesh.* – We consider a three-lozenge–based meshing of the hexagon in such a way that the quadrilateral/hexahedral finite elements we use for 2D/3D Cartesian meshes are readily available. Such a discretization of the hexagon along with the submeshing capabilities (local h-refinement) we have developed are illustrated in fig. 1.

3˙2. *Weak transport equation formulation over an element.* – Considering a finite element meshing $\boldsymbol{\mathcal{M}}_h$ of the domain $\boldsymbol{\mathcal{D}}$, the upwind DG scheme [8] leads to a weak formulation of eq. (1). More precisely, denoting $Q_p(\kappa)$ the space of polynomials of degree p or less on κ, the approximate flux

$$\phi_{n,h} = \phi_{n,h}|_\kappa \in V_h^p = \left\{v \in L^2(\boldsymbol{\mathcal{D}}) : \forall \kappa \in \boldsymbol{\mathcal{M}}_h, v|_\kappa \in Q_p(\kappa)\right\} \tag{3}$$

is the solution on an element κ of, $\forall \psi_h \in V_h^p$,

$$\begin{aligned} \int_\kappa \left(\vec{\Omega}_n \cdot \vec{\nabla}\phi_{n,h} + \Sigma_t \phi_{n,h}\right) \psi_h \mathrm{d}V - \int_{\partial\kappa_-} \left(\vec{n} \cdot \vec{\Omega}_n\right) \phi_{n,h}^+ \psi_h^+ \mathrm{d}s \\ = \int_\kappa Q_n \psi_h \mathrm{d}V - \int_{\partial\kappa_-} \left(\vec{n} \cdot \vec{\Omega}_n\right) \phi_{n,h}^- \psi_h^+ \mathrm{d}s, \end{aligned} \tag{4}$$

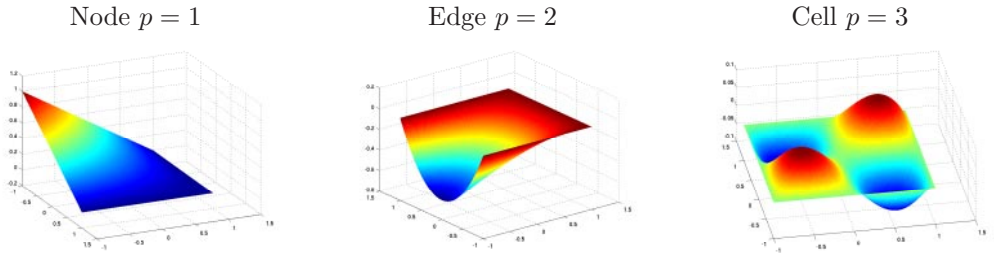

Fig. 2. – Some basis functions associated to the 2D quadrilateral element.

where the inflow boundary of κ is $\partial\kappa_- = \{\vec{r} \in \partial\kappa : \vec{\Omega} \cdot \vec{n}(\vec{r}) < 0\}$ and the interior $(+)$ and exterior $(-)$ boundary traces of $\phi_{n,h}$ on $\partial\kappa_-$ and $\partial\kappa_+$ are defined, respectively, by

$$\phi_{n,h}|^{\pm}_{\partial\kappa_-}(\vec{r} \in \partial\kappa_-) = \lim_{s \to 0^{\pm}} \phi_{n,h}\left(\vec{r} + s\vec{\Omega}_n\right);$$
$$\phi_{n,h}|^{\pm}_{\partial\kappa_+}(\vec{r} \in \partial\kappa_+) = \lim_{s \to 0^{\pm}} \phi_{n,h}\left(\vec{r} - s\vec{\Omega}_n\right).$$

As a consequence, $\phi_{n,h}$, in the element κ, can be computed in terms of the values of $\phi_{n,h}$ upstream the characteristic direction $\vec{\Omega}_n$ encountering $\partial\kappa$. In other words, $\phi_{n,h}$ can be calculated elementwise provided that the elements are suitably ordered according to $\vec{\Omega}_n$. In practice, for 2D core geometries based on hexagonal assemblies, six different cell orderings have to be considered depending on the sextant $\{\varphi \in]k\pi/3, (k+1)\pi/3[\}$, $\vec{\Omega}_n(\varphi, \mu)$ belongs to.

3˙3. *Hierarchical polynomial basis*. – For the easy development of p-enrichment capabilities, we consider hierarchical basis of $Q_p(\hat{\kappa})$ denoted $\Xi_p(\hat{\kappa}) = \{f_i\}_{i \in [1, \dim(Q_p(\hat{\kappa}))]}$, *i.e.* $\forall p \in \mathbb{N}^\star$,

$$\Xi_p(\hat{\kappa}) \subset \Xi_{p+1}(\hat{\kappa}). \tag{5}$$

The basis we have selected from [14] are based on a hierarchy of topological entities of nodes, edges, faces and cells that define the closure of an element. The j-th entity of dimension d belonging to the reference element $\hat{\kappa}$ closure $\bar{\hat{\kappa}}$ is denoted $M^d_{\hat{\kappa},j}$. The polynomial bases of any order p are obtained by associating shape functions to these entities with the property that any basis function associated to $M^d_{\hat{\kappa},j} \in \bar{\hat{\kappa}}$ vanishes over all lower-order bounding entities $M^{d' \leq d}_{\hat{\kappa},j'}$ except $M^d_{\hat{\kappa},j}$. For instance, the functions associated to an edge are null at the nodes and on the other edges of the element. This is of particular interest in our case while propagating the flux from one cell to the other through the boundary trace because it is straightforward to obtain $\phi_{n,h}|^{+}_{\partial\kappa^+}$ from $\phi_{n,h}|_{\kappa}$. Some of the resulting basis functions are depicted in fig. 2 in the case of the 2D quadrilateral element.

4. – Numerical results

In this section, the previous algorithm and the developed capabilities are illustrated by numerical results on two hexagonal core models. In both cases, rotational boundary conditions are used in order to reduce the spatial domain to one-third of the core.

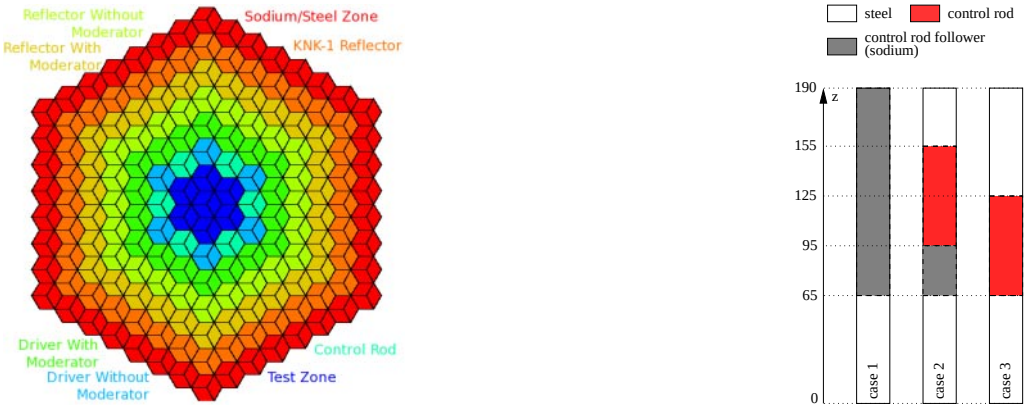

Fig. 3. – Takeda 3D hexagonal benchmark geometry and rod configurations.

4˙1. *KNK-II experimental reactor 3D benchmark.* – This benchmark, proposed in [15], is a four-energy group model of a fast spectrum sodium reactor. Three rod axial positions are considered as depicted in fig. 3. The Monte Carlo reference results were taken from [7] (obtained with the GMVP code). They are provided in terms of the effective multiplication factor k_{eff} and the material-averaged fluxes.

The angular and spatial convergences of our algorithm are summarized in the fully inserted rod case in tables I and II, respectively. The most noticeable effect concerns the spatial approximation order. Indeed, while the agreement between uniform 2nd and 3rd order is fairly good (-10 pcm on k_{eff}), some discrepancies in the control rod vicinity can be observed due to the largest flux variations induced by the absorber. We then consider

TABLE I. – *Angular convergence: $HQ_{3,4}$ compared to $HQ_{4,5}$ (uniform 2nd spatial order—case 3).*

Material	Material-averaged fluxes relative discrepancy (in %)			
	group 1	group 2	group 3	group 4
Test zone	≈ 0.0	0.002	-0.002	-0.014
Control rod	0.033	0.014	0.018	0.047
Axial blanket	-0.011	-0.002	0.001	0.003
Axial reflector	-0.015	≈ 0.0	0.003	0.005

TABLE II. – *Spatial p-convergence: uniform 2nd order (31941 d.o.f.'s) and variable 2nd/3rd order (36973 d.o.f.'s) compared to uniform 3rd order (75712 d.o.f.'s) ($HQ_{3,4}$ quadrature—case 3).*

Material	Material-averaged fluxes relative discrepancy (in %) (uniform order/variable order)			
	group 1	group 2	group 3	group 4
Test zone	-0.038 / ≈ 0.0	0.003 / -0.004	0.192 / -0.017	1.424 / -0.159
Control rod	-0.039 / -0.006	0.029 / 0.006	0.260 / 0.040	0.590 / 0.125
Axial blanket	0.119 / -0.055	0.012 / -0.059	-0.416 / -0.052	-1.068 / 0.173
Axial reflector	0.142 / -0.044	-0.027 / -0.061	-0.338 / -0.061	-0.767 / -0.035

TABLE III. – *Comparison against Monte Carlo reference—k_{eff} and CR reactivity worth.*

	k_{eff}			CR-worth (pcm)
	case 1	case 2	case 3	
Calculated value	1.09519	0.98344	0.87974	22361
Discrepancy (pcm)	+9	+14	−16	+61
σ^{MC} (pcm)	40	40	30	60

a non-uniform spatial approximation order with a local p-enrichment near the control rod (*i.e.* $p = 3$ in the test zone, control rod, driver with and without moderator, axial blanket and axial reflector regions, $p = 2$ elsewhere). One can see in table II that for a rather small increase in the computational cost, illustrated by the number of spatial degrees of freedom (d.o.f.'s), the discrepancies are largely reduced (−5 pcm on k_{eff}), even in the thermal region where the neutron flux is rather small.

Finally, the results with the $\text{HQ}_{3,4}$ quadrature and the variable 2nd/3rd spatial order are compared to the Monte Carlo reference in tables III and IV. In any case, the reactivity and the fluxes (except for the thermal region) are calculated within one standard deviation (σ^{MC}) of the Monte Carlo reference. This 3D benchmark illustrates the interest of the local p-enrichment capability that the DG spatial scheme offers.

4˙2. *h- and p-adaptiveness on a 2D benchmark.* – This second benchmark in 2D consists of the middle plane of the previous 3D core (case 3) [6] and is presented to introduce an ongoing work on h- and p-adaptiveness in the framework of this DG scheme. In order to fully benefit from the flexibility (in terms of local h- or p-refinement) of the DG scheme we have presented, adaptive algorithms have to be developed. Such techniques aim at obtaining an accurate solution with a lower computational cost than a uniform spatial mesh and order calculation. Two issues are involved in our case: finding an adequate error estimator for selecting the cells to be refined and setting-up an efficient adaptiveness mechanism within the three-loop iterative process solving the multigroup neutron transport equation. Here, in order to illustrate the convergence properties of the DG scheme in non-conforming meshes, a simple adaptation algorithm is considered; it uses an estimator based on some superconvergence properties of the DG scheme [16] and an iterative refinement procedure starting from a uniform DG scheme order (p) and uniform 3-lozenge–based hexagonal mesh. At each step, only the cells that verify $\varepsilon_\kappa > 0.5 \times \max_\kappa(\varepsilon_\kappa)$, where $\varepsilon_\kappa = \max_g(\sum_n w_n \varepsilon_\kappa^{g,n})$ and $\varepsilon_\kappa^{g,n}$ is the estimated value of $\|\phi_h^{g,n} - \phi_{\text{exact}}^{g,n}\|_{L^2(\kappa)}$, are considered for refinement. For the h-adaptive refinement

TABLE IV. – *Comparison against Monte Carlo reference—material-averaged fluxes (case 3).*

Material	Material-averaged fluxes relative discrepancy (in %)			
	group 1	group 2	group 3	group 4
Test zone	−0.384	−0.225	−0.242	−1.764
Control rod	0.084	0.195	0.423	0.443
Axial blanket	−0.192	0.615	−0.353	−0.797
Driver w/o moderator	−0.159	0.075	0.111	0.355

$\sigma^{\text{MC}} \approx 0.4$–$0.6\%$.

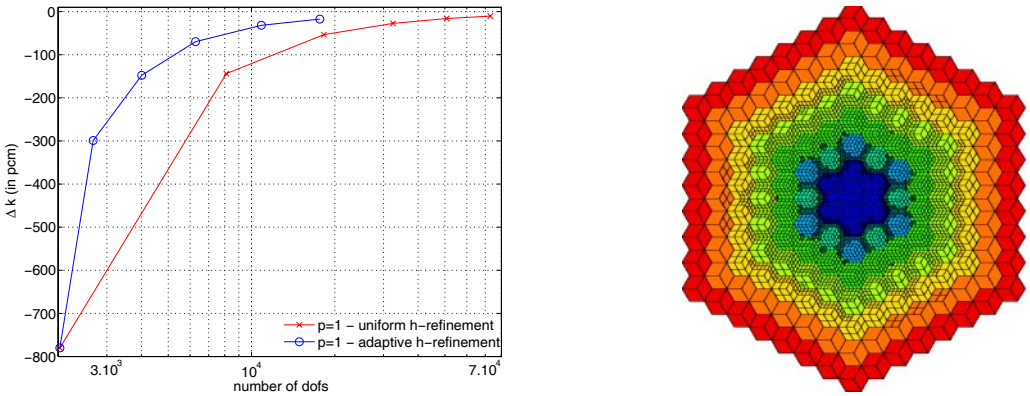

Fig. 4. – k_{eff} convergence and example of a non-conforming mesh obtained with the h-adaptive strategy.

strategy, the cell is split in 2×2 subcells while for the p-adaptive enrichment strategy, the cell order is increased by one. Note that a single spatial mesh is used for all the energy groups; this is not optimal as shown in [17].

In fig. 4, the h-adaptation is compared to a uniform mesh refinement for $p = 1$ in terms of k_{eff} as a function of *d.o.f.*'s. For a given accuracy, the number of *d.o.f.*'s is divided by ≈ 3 when adaptively refining the mesh (and so does the CPU time); in the $p = 2$ case (not shown), this factor goes up to ≈ 5. The example of a non-conforming mesh resulting from this adaptive algorithm is also presented in fig. 4: the refinement has been concentrated near the control rod and other important material interfaces in the central core region.

Finally, in fig. 5, various uniform and adaptive refinements are compared in terms of the group-averaged flux discrepancy in the control rod. One can see that for such a macroscopic quantity of interest and an accuracy of about 0.05%, h-refinement may become interesting over uniform p-enrichment only for $p > 1$ and adaptive p-enrichment gives the fastest convergence. While theoretical results show that the asymptotical con-

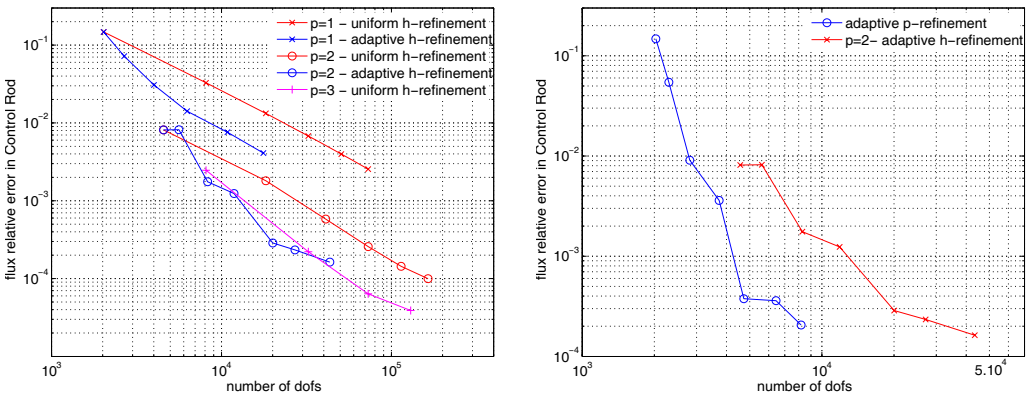

Fig. 5. – Convergence of the control-rod–averaged flux for various strategies.

vergence DG rate is limited by the angular flux regularity and does not benefit from a scheme order greater than $p = 1$; in practice, in the pre-asymptotic range, the use of a higher-order p (typically 2) largely improves the convergence and justifies the interest in combining both h- and p-adaptive techniques. See [18] and references therein for a discussion and a numerical illustration of the DG scheme asymptotic convergence rate.

5. – Conclusion

This paper has presented a numerical scheme for the modeling of geometries based on homogeneous hexagonal assemblies in the framework of the ERANOS code system dedicated to fast nuclear reactor analysis and design. The discrete ordinate method is used as angular approximation and the spatial discretization consists of discontinuous finite elements with variable order hierarchical polynomial basis over non-conforming meshes. A validation exercise on a 3D benchmark was used to demonstrate the soundness of these numerical methods. To illustrate an ongoing work on spatial adaptiveness, the interest of such an approach has been shown on a 2D benchmark with simple adaptive h-refinement and p-enrichment strategies.

REFERENCES

[1] Ruggieri J. M., Tommasi J., Lebrat J. F., Suteau C., Plisson-Rieunier D., De Saint Jean C., Rimpault G. and Sublet J. C., in *Proceedings of International Congress on Advances in Nuclear Power Plants ICAPP 2006*, edited by Anghaie S., Hong J., Pradel P. and Sasaki N. (American Nuclear Society, Reno) 2006.
[2] Palmiotti G., Lewis E. E. and Carrico C. B., Technical Report Argonne National Laboratory ANL-95/40, Argonne National Laboratory (1995).
[3] Schneider D. and Lautard J. J., in *Proceedings of International Conference on Mathematics and Computation, Reactors Physics and Environmental Analysis in Nuclear Applications M&C 2001* (American Nuclear Society, Salt Lake City) 2001.
[4] Hébert A., *Ann. Nucl. Energy*, **35** (2008) 363.
[5] Ikeda H. and Takeda T., *J. Nucl. Sci. Technol.*, **31** (1994) 497.
[6] Kim T. H. and Cho N. Z., *Ann. Nucl. Energy*, **23** (1996) 133.
[7] Lu H. and Wu H., *Nucl. Eng. Design*, **237** (2007) 230.
[8] Reed W. H. and Hill T. R., Technical Report Los Alamos National Laboratory LA-UR-73-479, Los Alamos National Laboratory (1973).
[9] Wareing T. A., McGhee J. M., Morel J. E. and Pautz S. D., *Nucl. Sci. Eng.*, **138** (2001) 256.
[10] Wang Y. and Ragusa J. C., *Ann. Nucl. Energy*, **36** (2009) 931.
[11] Gastaldo L., Le Tellier R., Suteau C., Fournier D. and Ruggieri J. M., in *Proceedings of International Conference on Mathematics, Computational Methods & Reactor Physics M&C 2009*, edited by Gamino R. (American Nuclear Society, Saratoga Springs) 2009.
[12] Lathrop K. D. and Carlson B. G., Technical Report Los Alamos National Laboratory LA-3186, Los Alamos National Laboratory, Los Alamos (1964).
[13] Le Tellier R. and Hébert A., *Nucl. Sci. Eng.*, **158** (2008) 28.
[14] Shephard M., Dey S. and Flaherty J., *Comput. Methods Appl. Mech. Eng.*, **147** (1997) 209.
[15] Takeda T. and Ikeda H., Technical Report OECD/NEA Committee on Reactor Physics NEACRP-L-330, OECD/NEA Committee on Reactor Physics (1991).
[16] Fournier D., Le Tellier R. and Suteau C., to be submitted to *Ann. Nucl. Energy*.
[17] Wang Y., Bangerth W. and Ragusa J., *Prog. Nucl. Energy*, **161** (2009) 22.
[18] Wang Y. and Ragusa J. C., *Nucl. Sci. Eng.*, **163** (2009) 56.